Large-Eddy Simulations of the 26 November 1991 FIRE II Cirrus Case

WILLIAM Y. Y. CHENG, TING WU, AND WILLIAM R. COTTON

Department of Atmospheric Science, Colorado State University, Fort Collins, Colorado

(Manuscript received 19 July 1999, in final form 25 September 2000)

ABSTRACT

Large-eddy simulations (LESs) were performed to study the dynamical, microphysical, and radiative processes in the 26 November 1991 FIRE II cirrus event. The LES model inherits the framework of the RAMS version 3b, developed at Colorado State University. It includes a new two-stream radiation model developed by Harrington and a new subgrid-scale model developed by Kosovic.

The LES model successfully simulated a single thin cloud layer for LES-1 and a deep cloud structure for LES-2. The simulations demonstrated that latent heat release can play a significant role in the evolution of thick cirrus clouds. For the thin cirrus in LES-1, the latent heat release was insufficient for the cirrus clouds to become positively buoyant. However, in some special cases such as LES-2, positively buoyant cells can be embedded within the cirrus layers. The updrafts from these cells induced its own pressure perturbations that affected the cloud evolution.

Vertical profiles of the total radiative and latent heating rates indicated that for well-developed, deep, and active cirrus clouds, radiative cooling and latent heating could be comparable in magnitude in the cloudy layer. This implies that latent heating cannot be neglected in the construction of a cirrus cloud model.

The probability density function (PDF) of the vertical velocity (w) was analyzed to assist in the parameterization of cloud-scale velocities in large-scale models. For the more radiatively driven, thin cirrus case, the PDFs are approximately Gaussian. However, in the interior of the deep, convectively unstable case, the PDFs of w are multimodal and very broad, indicating that parameterizing cloud-scale motions for such clouds can be very challenging.

1. Introduction

Although cirrus clouds are an important component of the climate system, they are not well understood. Cirrus clouds affect the global climate through the cloud–radiation feedback (Liou 1986). Because of our limited knowledge of the microphysical, radiational, and dynamical processes in cirrus clouds, numerical models of middle- and high-level clouds can be useful in determining the quantitative roles of dynamics, microphysics, and radiation in the life cycle of these clouds (Cotton and Anthes 1989).

In the middle of the 1980s, Starr and Cox (1985a,b) developed a two-dimensional model for simulating the evolution of cirrus clouds. Besides dynamical and thermodynamical processes (e.g., phase changes of water), effects due to the microphysical composition and the radiative processes were also explicitly incorporated into their model. They found that the structure of cirrus varied dramatically from nighttime to daytime because radiative processes affected the organization and bulk properties of the cloud. Simulations of thin cirrus under midday and nighttime conditions showed that with all other environmental factors being equal, daytime cirrus takes on a cellular structure with pockets of high ice water content (IWC) surrounded by regions of considerably lower IWC, while nighttime cirrus exhibits a more layered structure with less variation of IWC within a given layer. The simulated pattern of longwave radiative cooling above and warming below the cirrus cloud is the key factor in modulating the vertical stability, especially for nighttime cirrus. However, for daytime cirrus, the combination of longwave and shortwave radiation modulates not only the vertical stability but also the horizontal cloud structure. Pockets of high IWC enhance the absorption of solar radiation, warming the high IWC pockets, thus inducing more ascending motion (leading to a more cellular structure) than at nighttime.

Lilly (1988) proposed the application of radiative-convective mixed-layer models to cirrus clouds. Lilly ignored latent heating because in cirrus clouds, radiative heating is believed to be the primary source of destablization of the cloud layer, leading to the production of turbulent kinetic energy. Using a theoretically predicted radiative heating rate profile for a 2-km thick

Corresponding author address: William Cheng, Department of Atmospheric Science, Colorado State University, Fort Collins, CO 80523.
E-mail: cheng@atmos.colostate.edu

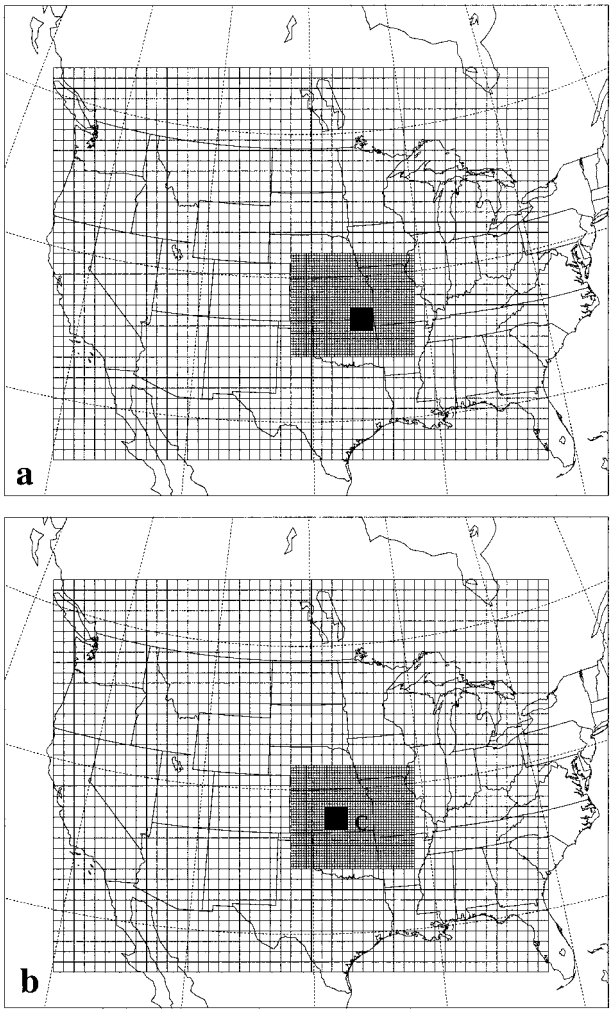

FIG. 1. The mesoscale grid configuration for (a) case 1 and (b) case 2. ''C'' denotes the location of Coffeyville, Kansas, the operational headquarters of the FIRE II field campaign.

cloud with its top at the level of the tropical tropopause (17 km) and with an IWC of 0.02 g m^{-3}, Lilly estimated the vertical velocity and timescales for radiatively induced cirrus turbulence. Lilly's results suggested that radiatively induced turbulence in cirrus could be comparable to the turbulence in boundary layer clouds.

The interaction of clouds with the general circulation is generally agreed to be the most important physical process requiring improvement in today's climate models. However, the current general circulation models (GCMs) that contain ice cloud (e.g., cirrus) parameterizations are very simplistic (e.g., fixed ice crystal size and geometry) (Kristjánsson et al. 2000).

Since cirrus clouds are located high above the planetary boundary layer (PBL), turbulent kinetic energy (TKE) dissipation due to friction may not be as important as horizontal redistribution through wave activities. Vertical redistribution of TKE is suppressed due to stable stratification of the environmental atmosphere.

TABLE 1. Model setups for mesoscale grids in case 1 and case 2. The vertical grid spacing is the same for every grid.

	Case 1	Case 2
Number of grids	4	3
x grid points	50, 50, 47, 46	50, 50, 47
y grid points	40, 42, 47, 46	40, 42, 47
z grid points	65, 65, 65, 65	65, 65, 65
Horizontal grid spacings (km)	80, 20, 4, 1	80, 20, 4
Vertical grid spacings (m)	200 to 500	200 to 500

These features may imply that the motion of cirrus clouds may be quasi–two-dimensional (Gultepe and Starr 1995a,b). Also, the turbulent parameterization schemes developed for boundary layer processes may not be applicable to cirrus clouds due to the marked difference in forcing mechanisms (e.g., boundary layer clouds are influenced by the earth's surface) (Stull 1988).

This article is a first attempt to examine the dynamical, microphysical, and radiative processes in cirrus clouds using large eddy simulation (LES). In LES, the large eddies are simulated while the small eddies are parameterized (Meong 1984). Two cases were chosen from the mesoscale simulation (Wu 1999) of a cirrus cloud event during FIRE II (FIRE is the First ISCCP Regional Experiment; ISCCP is the International Satellite Cloud Climatology Project). The FIRE II campaign, with headquarters in Coffeyville, Kansas (marked by ''C'' in Fig. 1b), gathered field data from November to December 1991 in an attempt to better understand the radiational, dynamical, and microphysical processes in cirrus clouds. The December 1995 issue of the *Journal of the Atmospheric Sciences* contains many articles on FIRE II results.

2. Mesoscale simulation

The cirrus event of interest occurred on 26 November 1991 during FIRE II (Mace et al. 1995). The synoptic setting of the cirrus event was characterized by a small amplitude upper-level trough-ridge system over North America on 26 November 1991, with northwesterly flow in the upper-levels ahead of the offshore ridge over the West Coast, and a broad diffluent trough in the central United States. The exit region of a strong upper-level northwesterly jet, covering a third of the western United States, contributed to the development of the cirrus cloud system in this study. A more detailed description of this cirrus event can be found in Mace et al. (1995).

Two mesoscale simulations were performed with RAMS (Pielke et al. 1992) version 3b (case 1 and case 2). Each uses the same two coarsest grids (Fig. 1 and Table 1), but the location of the third grid was different. An additional fourth grid was used in case 1. Our strategy is to conduct a mesoscale simulation of the cirrus event. Once we have verified our mesoscale model results against available observations, data from each me-

soscale simulation will be used to initialize and force (nudge) an LES at very fine resolution (LES-1 and LES-2, respectively).

The mesoscale model used a new two-moment microphysical scheme (Harrington et al. 1995; Meyers et al. 1997) coupled to the Harrington (1997) two-stream radiation package (see also Harrington et al. 1999) to predict the mixing ratios and number concentrations of pristine ice crystals, snow, and aggregates. In addition, through the coupling with the two-moment cloud microphysics, the two-stream radiation model accounts for the ice habit (the nonsphericity) of the ice particles in the radiative transfer equations. In addition, the two-stream radiation model accounts for the effects of water vapor, ozone and carbon dioxide, and the optical effects of various hydrometeor species. The Harrington radiation scheme uses the Lorenz–Mie theory to calculate the optical properties of water drops, and the theories of Mitchell and Arnott (1994) and Mitchell et al. (1996) are used for nonspherical ice crystals.

Snow is defined as relatively large ice particles (125–10 000 μm) that grew from pristine ice via vapor deposition and may continue to grow by riming and vapor deposition (Harrington et al. 1995). Aggregates are defined as ice particles formed by collision and coalescence of pristine ice, snow, and/or other aggregates (Meyers et al. 1997). Meyers et al. (1997) have shown that in an idealized convective case, the mean diameter evolved more realistically in a two-moment scheme than in a single-moment scheme (Walko et al. 1995).

In the two-moment RAMS cloud microphysics scheme, the number concentration tendency equation contains advection, turbulent (resolved and subgrid scale) transport, sedimentation, and source/sink terms accounting for various microphysical processes. Both homogeneous (DeMott et al. 1994) and heterogeneous ice nucleation (Meyers et al. 1992) are allowed. The RAMS assumes a modified gamma distribution for the size distribution, with the shape parameter ν at 2 (see Meyers et al. 1997). In addition, the microphysics module parameterizes the effect of secondary production of ice crystals due to the rime-splinter process. The RAMS does not track the history of each individual ice particle. However, at each time step, the model diagnoses the ice crystal habit according the the temperature and ice supersaturation at each grid point. Pristine ice or snow can be columns, hexagonal plates, dendrites, needles, or rosettes, and the shape of the ice crystal is accounted for by the capacitance. It is well known that ice crystals in the real world are often irregularly shaped (Gultepe et al. 2000), but the model cannot account for this. Nevertheless, the microphysical and radiational processes are reasonably well represented by accounting for the variable ice habit at each time step.

The model initial and boundary conditions were provided by the Mesoscale Analysis and Prediction System (MAPS) (Benjamin et al. 1991) and enhanced with National Weather Service rawinsonde soundings. The model was initialized at 0000 UTC 26 November 1991.

TABLE 2. Vertical levels (z_*) used in the mesoscale simulations (in m).

0.0	300.0	600.0	900.0	1200.0	1500.0
1800.0	2100.0	2400.0	2700.0	3000.0	3300.0
3600.0	3900.0	4100.0	4300.0	4500.0	4700.0
4900.0	5100.0	5300.0	5500.0	5700.0	5900.0
6100.0	6300.0	6500.0	6700.0	6900.0	7100.0
7300.0	7500.0	7700.0	7900.0	8100.0	8300.0
8500.0	8700.0	8900.0	9100.0	9300.0	9500.0
9700.0	9900.0	10 100.0	10 300.0	10 600.0	10 900.0
11 200.0	11 500.0	11 800.0	12 200.0	12 600.0	13 000.0
13 400.0	13 800.0	14 200.0	14 600.0	15 000.0	15 500.0
16 000.0	16 500.0	17 000.0	17 500.0	18 000.0	

Figure 1 shows the grids for the mesoscale simulations. Although grids 1 and 2 were the same for case 1 and case 2, the finer grids were different. In case 1, we attempt to capture the fine-scale features of a thin cirrus cloud located in the southeast quadrant of grid 2, while in case 2, we attempt to capture the fine-scale features of a thicker and more convective cirrus cloud in the northwest quadrant of grid 2. The grid configurations for case 1 and case 2 are given in Tables 1 and 2. The model terrain-following vertical coordinate (z_*) is defined by $z_* = H[(z - z_s)/(H - z_s)]$, where H is the height of the model top, z_s is the terrain height, and z is the height above sea-level (Tripoli and Cotton 1982).

Figure 2 shows the 500-hPa geopotential height at 24 h (0000 UTC 27 November 1991) into the simulation from grid 1 as well as the 500-hPa geopotential height from the MAPS analysis. The model appeared to capture the large-scale trough-ridge pattern reasonably well. From the simulated 7600-m (above sea level) total ice concentration (pristine ice, snow, aggregates) of grid 2, in Fig. 3a, we can see that the model reproduced cloud bands that could be identified with high cloud visible optical depth maxima derived from satellite data (Mace et al. 1995) in Fig. 3c. However, the simulated case 1 (case 2) thin (thick) cirrus band was more to the northwest, as compared to the derived satellite data. As discussed in Wu (1999), observations have shown that the leading edge of the observed cloud system was composed of a shallow and high cloud layer (case 1), and the cloud layer to the northwest of the leading edge was deep with middle-level clouds underneath the highest cirrus clouds (case 2). In addition, the model-derived cloud optical depth (solar band 3: 0.245–0.7 μm; Fig. 3b) from the two-stream radiation scheme compared very favorably to the results of Mace et al. (1995). Although a thick cirrus (in the mesoscale simulation) near the eastern Colorado cannot be matched with observations, RAMS showed sufficient skill in reproducing thin (case 1) and thick (case 2) cirrus clouds. Therefore, we can use the mesoscale model results to drive the LES.

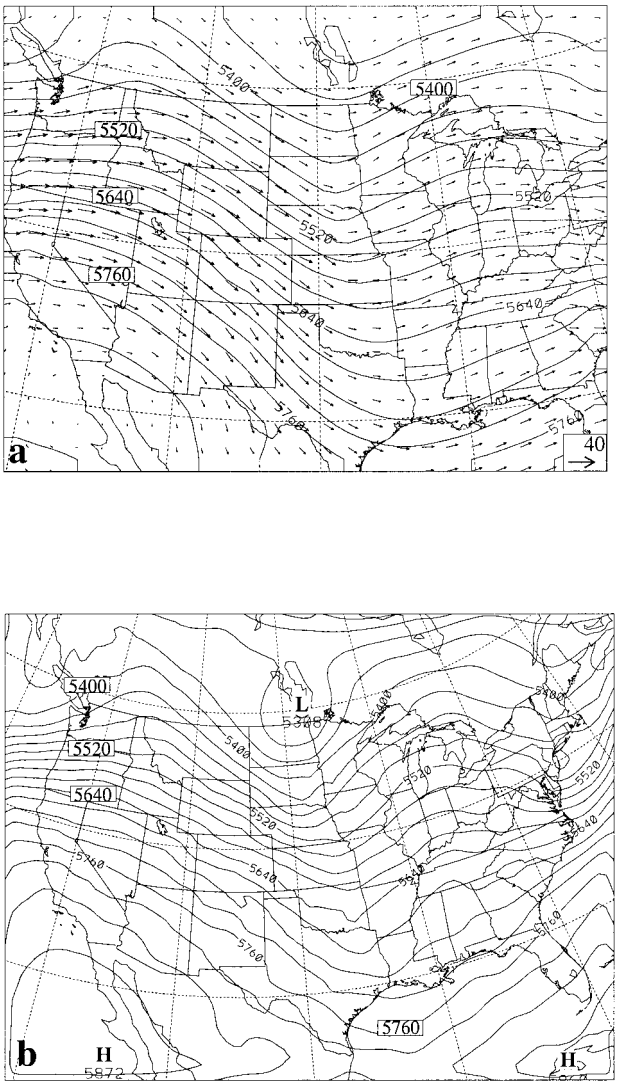

FIG. 2. (a) 24-h predicted 500-hPa geopotential height (at contour intervals of 30 m) superposed with 500-hPa wind vectors (m s^{-1}) from grid 1 of the mesoscale simulation (0000 UTC 27 Nov 1991). Inset indicates the scale of the horizontal wind vectors (m s^{-1}), (b) 500-hPa geoptential height (at contour intervals of 30 m) from MAPS analysis at 0000 UTC 27 Nov 1991.

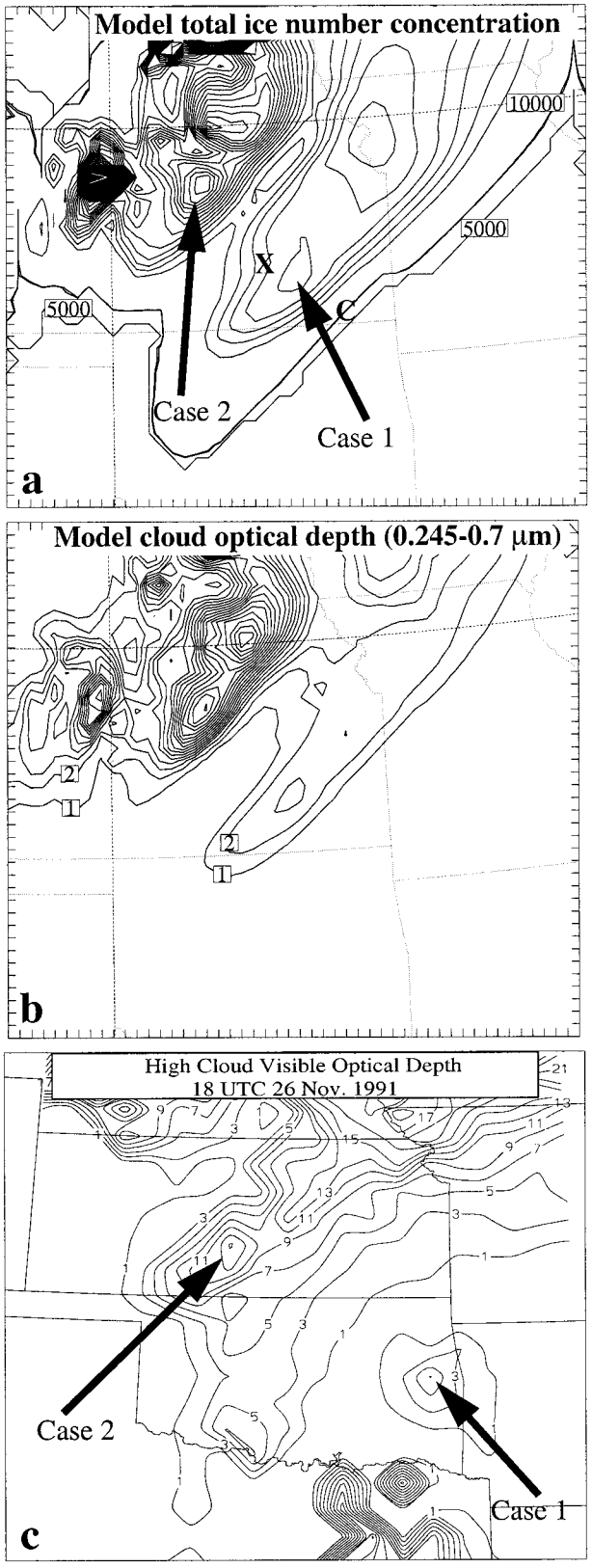

→

FIG. 3. (a) Mesoscale model (grid 2) 7600-m (ASL) total ice crystal number concentration at 18 h into the simulation (1800 UTC 26 Nov 1991) at contour intervals of 5000 kg^{-1}; (b) mesoscale model (grid 2) cloud optical depth (solar band 3: 0.245–0.7 μm) computed from the two-stream radiation code at contour intervals of every 1 unit at the same time as (a); (c) high cloud visible optical depths derived from GOES data at 1800 UTC 26 Nov 1991 [(c) taken from Mace et al. 1995]. ''C'' denotes the location of Coffeyville, Kansas, the operational headquarters of the FIRE II field campaign. ''X'' denotes the center of the LES grid.

3. The subgrid-scale (SGS) model

The LES model inherits the framework of the Colorado State University RAMS version 3b (Pielke et al. 1992), with a two-stream radiation scheme by Harrington (1997; see also Harrington et al. 1999) and an SGS model by Kosovic (1996). The SGS model represents a critical component of a successful LES. The commonly used linear SGS models result in erroneous mean velocity profiles in simulations of neutrally and stably stratified atmospheric boundary layers (Kosovic 1996, 1997). In addition, linear models are absolutely dissipative, resulting in relaminarization of the flows if subjected to strong stable stratification (Kosovic 1996). Since cirrus clouds in midlatitudes are generally associated with a stably stratified and strongly sheared atmospheric environment, we felt that Kosovic's SGS model, capable of reproducing the energy backscatter as well as the effects of SGS anisotropy characteristics of shear-driven flows, was more suitable for this study.

According to Kosovic's (1996) nonlinear model, the SGS stress is defined as

$$M_{ij} = -(C_s\Delta)^2\left[2(2S_{mn}S_{mn})^{0.5}S_{ij} + C_1\left(S_{ik}S_{kj} - \frac{1}{3}S_{mn}S_{mn}\delta_{ij}\right) + C_2(S_{ik}\Omega_{kj} - \Omega_{ik}S_{kj})\right], \quad (1)$$

where C_s is the traditional Smagorinsky constant, which is defined as

$$C_s = \left[\frac{8(1 + C_B)}{27\pi^2}\right]^{0.5}; \quad (2)$$

δ_{ij} is the Kronecker delta (a scalar quantity that is equal to 1 when $i = j$ and 0 otherwise); and Δ is the length scale defined by Moeng (1984) as

$$\Delta = (\Delta x\Delta y\Delta z)^{1/3}, \quad (3)$$

where Δx, Δy, and Δz are the grid spacings in x, y, and z directions, respectively.

Kosovic suggested that

$$C_B = 0.36. \quad (4)$$

The quantities S_{ij} and Ω_{ij} are strain rate tensor and rotation rate tensor, respectively:

$$S_{ij} = \frac{1}{2}\left(\frac{\partial u_i}{\partial x_j} + \frac{\partial u_j}{\partial x_i}\right), \quad (5)$$

$$\Omega_{ij} = \frac{1}{2}\left(\frac{\partial u_i}{\partial x_j} - \frac{\partial u_j}{\partial x_i}\right), \quad (6)$$

where u_i and u_j are the model wind components.

The nonlinear model parameters C_1 and C_2 are determined so that the model provides the correct energy transfer and captures the normal stress effects observed in sheared flows. The following values for C_1 and C_2 are suggested by Kosovic (1996):

$$C_1 = \frac{31C_B}{7(1 + C_B)S(k_c)} \quad (7)$$

$$S(k_c) = 0.5, \qquad C_1 = C_2. \quad (8)$$

4. Nudging the LES model

Generally, horizontally homogeneous initialization is used in an LES because of the small horizontal model domain. Like cloud-resolving models of tropical deep convection (Moncrieff et al. 1997), cirrus clouds are strongly influenced by larger-scale motions. We thus chose to perform a mesoscale simulation of RAMS and then to use the mesoscale model output to construct large-scale tendencies for the LES.

The nudging algorithm used takes the following form:

$$u(k, i, j, t) = u(k, i, j, t - 1) + F_{\text{model}} + G[u_{\text{obs}}(k) - \overline{u}(k, t - 1)], \quad (9)$$

where $u(k, i, j, t)$ is the model predicted u value at the current timestep; $u(k, i, j, t - 1)$ is the model u value at the previous timestep; model-forcing terms (F_{model}) included advection, diffusion, buoyancy, etc.; u_{obs} is the value of u being nudged to and is a function of the vertical index k; $\overline{u}(k, t - 1)$ is the horizontal average of u at the previous timestep; and G is the inverse of the nudging timescale. Because the nudging contribution is artificial, it must not be a dominant term in the governing equations and should be scaled by the slowest physical adjustment process in the model. Of note, using $\overline{u}$ instead of u in the above equation avoids nudging out the fine scale features in the LES.

To apply nudging, u_{obs} was calculated from the mesoscale simulation outputs by using a linear interpolation method. In this study, nudging was performed for the three-dimensional wind components (u, v, and w), perturbation Exner function (π'), perturbation ice–liquid–water potential temperature (θ'_{il}), and total water mixing ratio (r_t). In addition, nudging was only applied to the five outermost grid points on the lateral boundaries.

5. Initialization and boundary conditions

The LES model was initialized with a sounding taken from the mesoscale simulation described earlier. The sounding profiles used in the LES studies are shown in Fig. 4. One of these two soundings was taken from a shallow cloud band near the leading edge of the simulated mesoscale cirrus cloud system (LES-1; corresponding to case 1 in Fig. 3), while the other sounding is taken from a deep cloud layer northwest of the simulated mesoscale cloud (LES-2; corresponding to case 2 in Fig. 3).

The two 3D LES runs to be discussed in this article were designed to simulate the dynamical, microphysical, and radiative processes in both shallow and deep ice

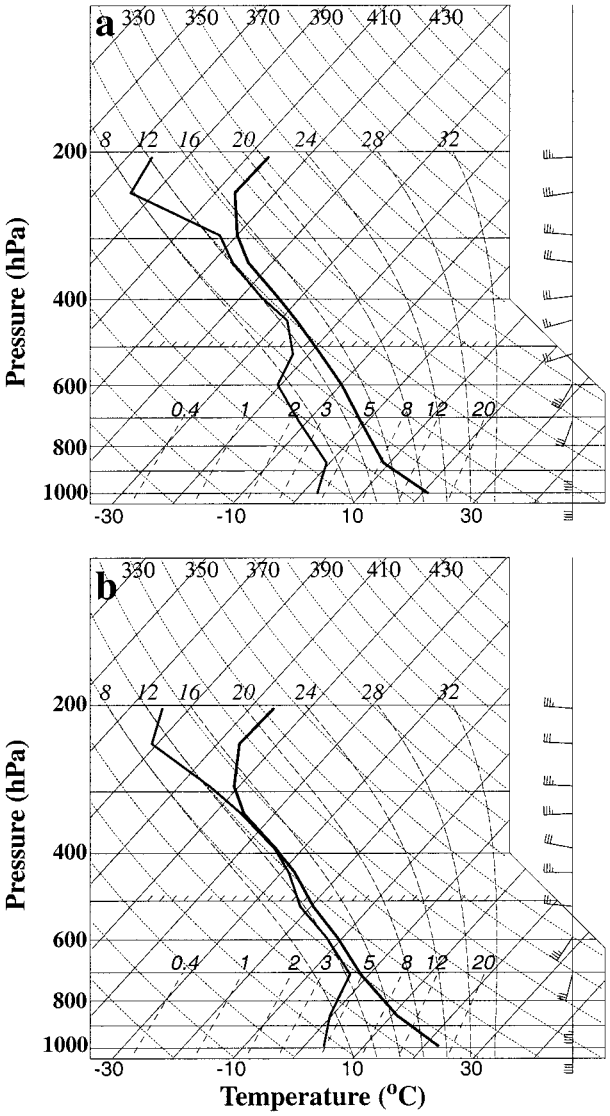

FIG. 4. Skew *T*–log*p* diagram for temperature (°C), dewpoint temperature (°C), and wind (m s^{-1}) at (a) 1700 UTC 26 Nov 1991 and (b) 1930 UTC 26 Nov 1991 taken from the finest grids of cases 1 and 2, respectively, in the mesoscale simulation (Fig. 1). The soundings in (a) and (b) are the initial conditions of LES-1 and LES-2, respectively. A full (half) barb is 5 (2.5) m s^{-1}.

cloud systems to obtain greater insight into the dynamics and physics of the observed cirrus cloud event.

A much finer grid mesh was used for the LES, with $\Delta x = \Delta y = 150$ m. The term Δz varied from 50 m (within the cloud layer from 6 to 10 km) to 400 m (near the surface). The model had a horizontal extent of 5.85 km $\times$ 5.85 km and a height of 11.4 km (115 vertical levels, see Table 3). The center of the LES grid is marked by ''X'' in Fig. 3a. The same grid configuration was used for both cases. The horizontal boundary conditions were cyclic. It should be pointed out that the lateral cyclic boundary conditions were independent of the nudging (discussed in the previous section), which

TABLE 3. Vertical levels (z_*) used in LES (in m).

0.0	400.0	800.0	1200.0	1600.0	2000.0
2400.0	2800.0	3200.0	3500.0	3800.0	4100.0
4400.0	4600.0	4800.0	5000.0	5100.0	5200.0
5300.0	5400.0	5500.0	5600.0	5700.0	5800.0
5900.0	6000.0	6050.0	6100.0	6150.0	6200.0
6250.0	6300.0	6350.0	6400.0	6450.0	6500.0
6550.0	6600.0	6650.0	6700.0	6750.0	6800.0
6850.0	6900.0	6950.0	7000.0	7050.0	7100.0
7150.0	7200.0	7250.0	7300.0	7350.0	7400.0
7450.0	7500.0	7550.0	7600.0	7650.0	7700.0
7750.0	7800.0	7850.0	7900.0	7950.0	8000.0
8050.0	8100.0	8150.0	8200.0	8250.0	8300.0
8350.0	8400.0	8450.0	8500.0	8550.0	8600.0
8650.0	8700.0	8750.0	8800.0	8850.0	8900.0
8950.0	9000.0	9050.0	9100.0	9150.0	9200.0
9250.0	9300.0	9350.0	9400.0	9450.0	9500.0
9550.0	9600.0	9650.0	9700.0	9750.0	9800.0
9850.0	9900.0	9950.0	10 000.0	10 100.0	10 200.0
10 300.0	10 400.0	10 600.0	10 800.0	11 000.0	11 200.0
11 400.0					

represented an additional tendency term. The model top was a rigid lid with a Rayleigh friction layer to prevent gravity wave reflection from the upper boundary. The lower surface, which is not as important for cirrus clouds as it is for convective storms, was a material surface across which fluxes of heat, moisture, and momentum were solved following a theory proposed by Louis (1979).

6. LES results: LES-1 (a shallow cloud system)

a. Simulation overview

The LES-1 covered a 2-h 3D simulation period, which was initialized with a sounding taken at 1700 UTC 26 November 1991 (Fig. 4a) from the finest grid of case 1 in the mesoscale simulation (Fig. 1a). Snapshots of the vertical cross sections (at $X = -0.08$ km) of pristine ice (PI) number concentration, snow number concentration, and vertical velocity at 1730, 1800, and 1900 UTC are shown in Figs. 5–7. The predicted cloud system had an apparent single cloud layer from total ice mixing ratio, r_{ice} (includes pristine ice, snow, and aggregates), in Fig. 8b even though some secondary peaks in both PI and snow number concentrations were discernible (Figs. 5 and 6). Both particle number concentration and mixing ratio were higher near the cloud top levels than in the levels below. The maximum PI concentration, PI mixing ratio, snow concentration, and snow mixing ratio were about 0.6 L^{-1}, 2.1 $\times$ 10^{-4} g kg^{-1}, 0.12 L^{-1}, and 8.0 $\times$ 10^{-4} g kg^{-1} (figure not shown), respectively. The low hydrometeor concentrations and mixing ratios in PI and snow were attributed to small vertical velocity (see below).

As can be seen from the plots of vertical velocity (Fig. 7), the cloud system was composed of cells of upward and downward motion. The horizontal extent of the cells ranged from less than 1 km to as large as 3.5

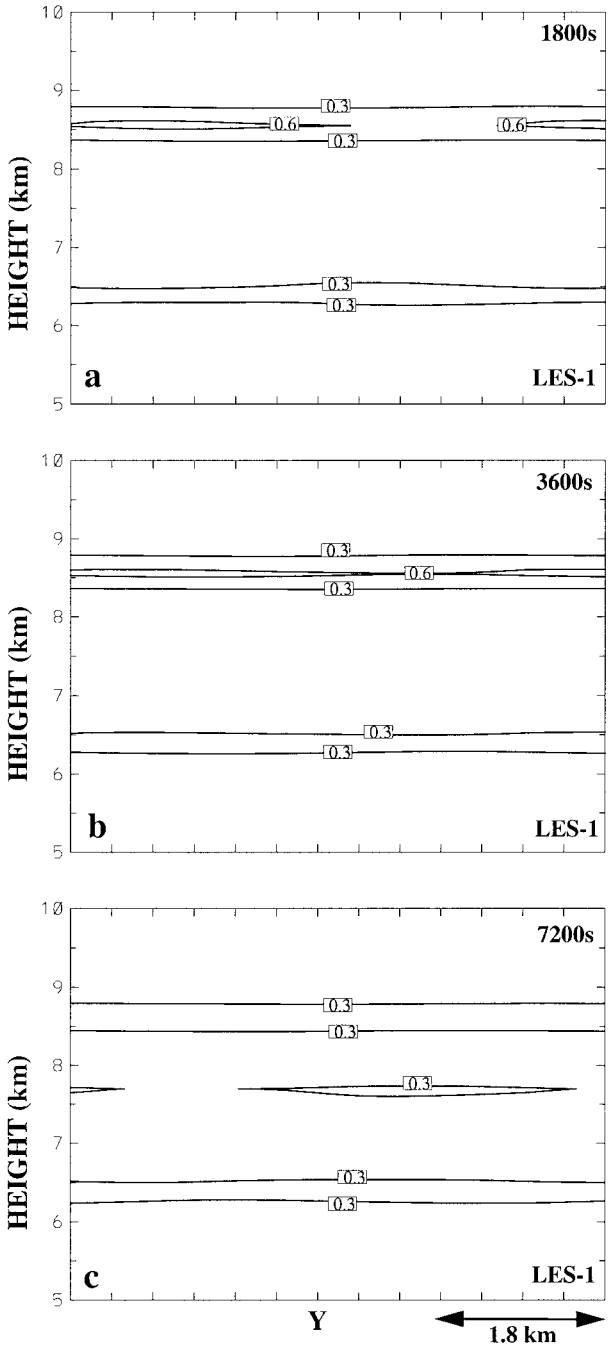

FIG. 5. Vertical *y*–*z* cross section (at $x = -0.08$ km) of pristine ice number concentration (at contour intervals of 0.3 L^{-1}) for LES-1 at (a) 30 min, (b) 60 min, and (c) 120 min into the simulation. The horizontal length of the cross section is 5.85 km, and the distance between each tick mark in the horizontal is 0.45 km. The same horizontal scale applies for all vertical cross sections in this paper.

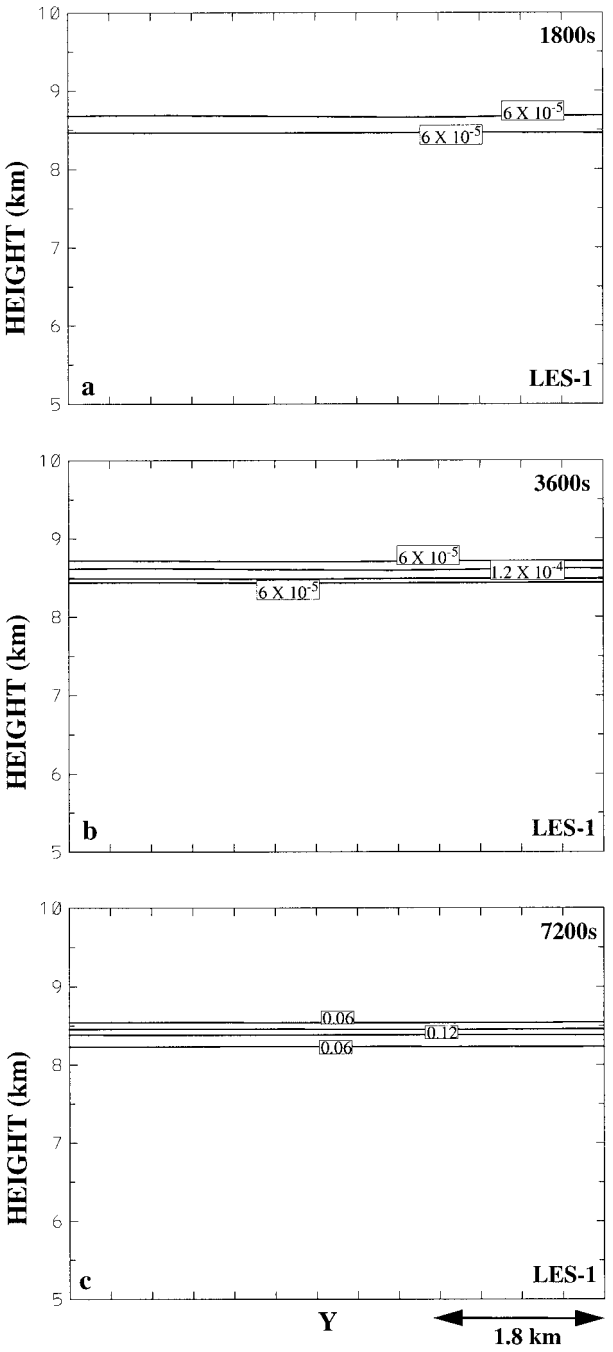

FIG. 6. Vertical *y*–*z* cross section (at $x = -0.08$ km) of snow particle number concentration for LES-1 at (a) 30 min (at contour intervals of 6×10^{-5} L^{-1}), (b) 60 min (at contour intervals of 6×10^{-5} L^{-1}), and (c) 120 min (at contour intervals of 0.06 L^{-1}) into the simulation.

km. Vertical extent of the cells were generally less than 1 km. The greater horizontal extent of these cloud cells (cells in the horizontal cross sections) may imply that the cloud system was modulated by shear-driven turbulence (Stull 1988). The sizes of these embedded cells were similar to those found in observational studies (Starr and Wylie 1990; Gultepe et al. 1995). The vertical velocity was on the order of several centimeters per second, similar to the thin cirrus cloud simulated by Starr and Cox (1985a) and within the typical range of vertical velocity reported in Heymsfield's (1977) observational study.

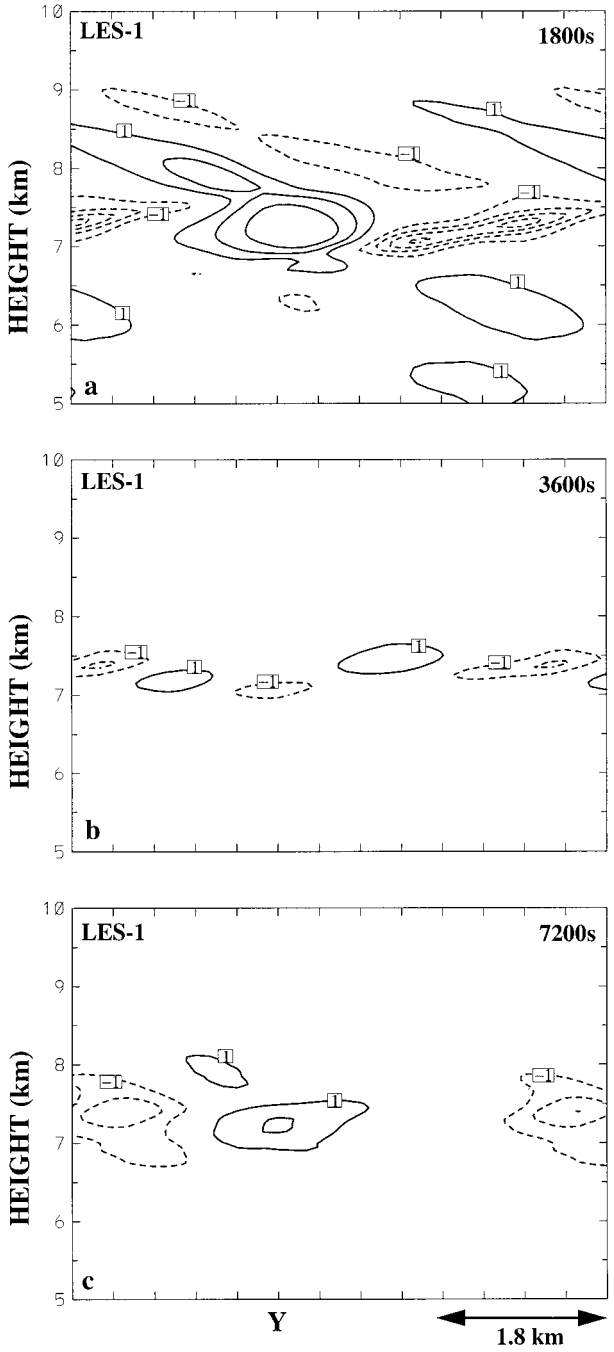

FIG. 7. Vertical y–z cross section (at $x = -0.08$ km) of vertical velocity (w; at contour intervals of 1 cm s^{-1}) for LES-1 at (a) 30 min, (b) 60 min, and (c) 120 min into the simulation. Zero-contour suppressed for the sake of clarity.

Horizontally averaged total water mixing ratio (r_t), total ice mixing ratio (r_{ice}), ice–liquid–water potential temperature (θ_{il}), and potential temperature (θ) at 60 min into the simulation are shown in Fig. 8. A single layer of total ice mixing ratio maximum was predicted just below the 9000-m level, with a depth of slightly more than 500 m. The maximum horizontally averaged total ice mixing ratio was on the order of 1.0×10^{-4} g kg^{-1} throughout the simulation (figure not shown). Again, the low total ice mixing ratio was due to the small vertical velocity. Below the single cloud layer, the profiles of θ_{il} and θ indicated a nearly neutral layer of about 1 km deep between 7- and 8-km levels. Although the hydrometeor concentrations were a bit too low, nevertheless, we have captured the essential features of this thin cirrus case in the model.

As mentioned earlier, RAMS diagnoses the ice crystal habit at each time step but does not keep track of the history of individual ice crystals. However, examining the ice crystal habits at various times can give insight into the environmental conditions in which the ice crystals grew. For LES-1, about two thirds of the pristine ice grew via the column mode, and about a third grew by the needle mode, with less than 1% growing by hexagonal plate mode throughout the entire simulation (Table 4). The snow particles grew almost exclusively via the column mode, with less than 1% growing by needle mode throughout the entire simulation (Table 5). This is an indication that almost all of the snow particles and two thirds of the PI were subjected to low ice supersaturation. The median diameter of the snow particles reached a maximum of 180 μm in the interior of the cloud after 2 h of integration (figure not shown), close to the value of another case of cirrus cloud over Coffeyville at 25 November 1991 (Heymsfield et al. 1998).

Vertical profiles of horizontally averaged TKE at 30, 60, and 120 min into the simulation are shown in Fig. 9a. We defined TKE as

$$\text{TKE} = \frac{1}{2}(u'^2 + v'^2 + w'^2) \qquad (10)$$

where u' is the x-velocity deviation from the horizontal mean at a particular level. A similar definition holds for v' and w'. As the cloud developed, the TKE (albeit small) increased in the early stage, with a peak in TKE slightly less than 0.003 m^2 s^{-2}. The peak TKE was the same order of magnitude as the simulation by Starr and Cox (1985a). The TKE decreased as the cloud evolved into its mature stage. By the end of the simulation, the maximum horizontally averaged TKE within the cloud layer was only about 0.0012 m^2 s^{-2}. In addition, from Fig. 9b, most of the TKE resides in the horizontal, indicating a quasi–two-dimensional flow regime.

Infrared radiative cooling throughout the cloud layer was largely compensated by solar warming, resulting in a maximum cooling of only about 0.05 K day^{-1} near the cloud top (Fig. 10a). Figure 10b also show that both solar and infrared optical extinction peaked at about 8.5 km, where the maximum number concentration of ice particles was predicted. Below this level, the solar and infrared optical extinction were much smaller because of the smaller ice particle number concentration and mixing ratio.

In Fig. 11, vertical profiles of the horizontally aver-

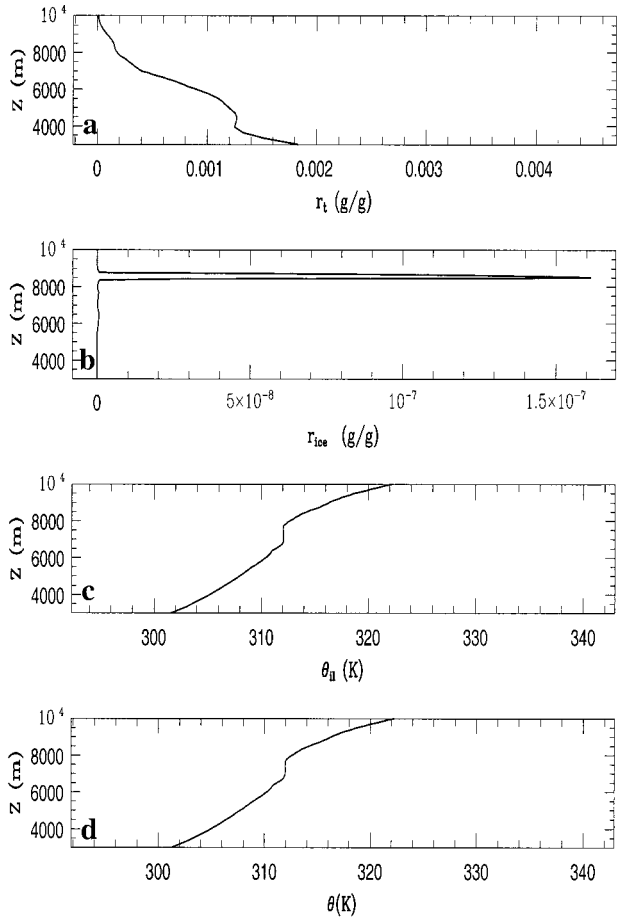

FIG. 8. Profiles of horizontally averaged (a) total water mixing ratio (r_t), (b) total ice mixing ratio (r_{ice}), (c) ice–liquid–water potential temperature (θ_{il}), and (d) potential temperature (θ) at 60 min into the simulation for LES-1.

aged heating rates due to total radiative processes and latent heat release associated with phase change of water are shown for LES-1. The latent heating rates mainly peaked at three levels, indicating a layered cloud structure commonly observed within cirrus clouds (Mace et al. 1995), especially *passive cirrus* (to be discussed later). The overall latent heating rate in the cloud system

TABLE 4. LES pristine ice habit. Cl for columns, Ndl for needles, Hpl for hexagonal plates, Den for dendrites, and Ros for rosettes.

Model time (min)	Cl	Ndl	Hpl	Den	Ros
LES-1					
30	64.4%	34.7%	0.9%	0%	0%
60	64.7%	34.4%	0.9%	0%	0%
120	63.2%	35.9%	0.9%	0%	0%
LES-2					
30	4.7%	0.5%	0.1%	0%	94.7%
60	71.0%	0.8%	0%	0%	28.2%
120	99.997%	0%	0.003%	0%	0%

TABLE 5. LES snow habit. Cl for columns, Ndl for needles, Hpl for hexagonal plates, Den for dendrites, and Ros for rosettes.

Model time (min)	Cl	Ndl	Hpl	Den	Ros
LES-1					
30	99.4%	0.6%	0%	0%	0%
60	99.6%	0.4%	0%	0%	0%
120	100%	0%	0%	0%	0%
LES-2					
30	9.6%	33.4%	0%	0%	57.0%
60	61.5%	27.8%	1.5%	0%	9.2%
120	59.0%	23.1%	17.9%	0%	0%

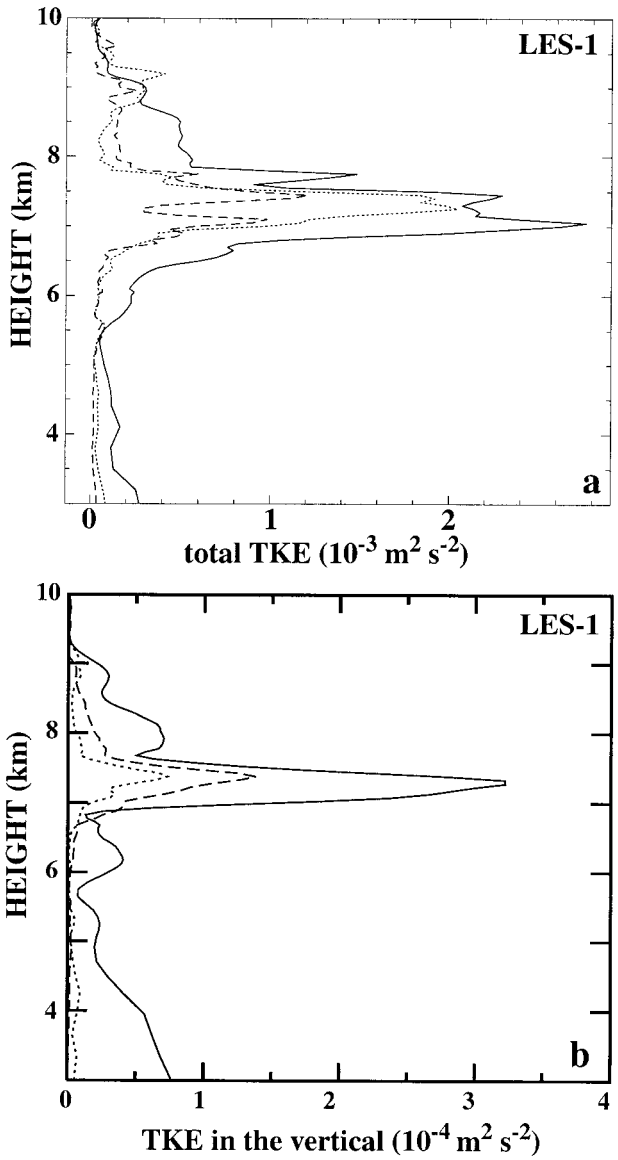

FIG. 9. (a) Profiles of horizontally averaged total turbulent kinetic energy (TKE) at 30 min (solid), 60 min (dotted), and 120 min (dashed); (b) profiles of horizontally averaged turbulent kinetic energy in the vertical ($\frac{1}{2}\langle w'w'\rangle$) at 30 min (solid), 60 min (dotted), and 120 min (dashed) into the simulation for LES-1.

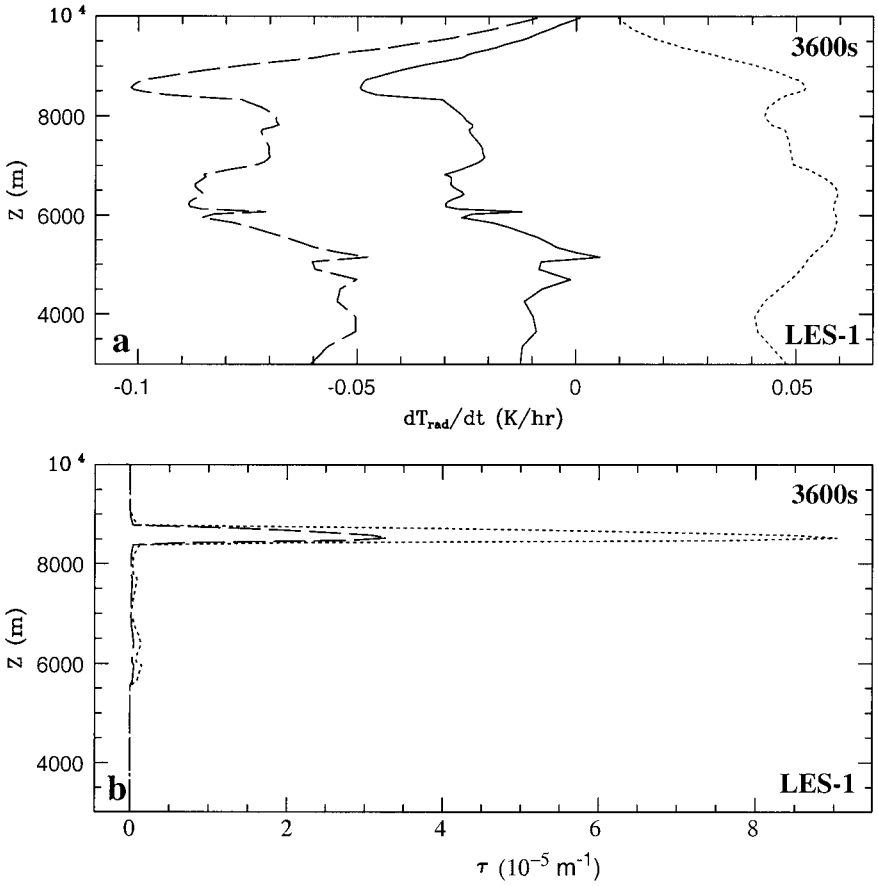

FIG. 10. (a) Profiles of radiative heating rate (solid line: total; dashed line: IR; dotted line: solar) and (b) solar (τ_{solar}) and infrared (τ_{infrared}) optical extinctions (dashed line: IR; dotted line: solar) at 60 min into the simulation for LES-1.

was much smaller in magnitude than the radiative cooling effect, a finding similar to an observational study of a stable cirrus cloud in Gultepe and Rao (1993). No obvious net evaporation at any level was seen in this case during the first 2-h simulation. The net radiative cooling was much stronger throughout most of the cloud system than latent heating, indicating that this cirrus case was mostly driven by radiation. Strong radiative cooling occurred throughout most of the cloud layer, with a shallow radiative warming layer centered at about 5.2 km.

b. Probability density function (PDF) of w

Since the vertical velocity distribution is critical in the parameterization of cloud-scale physics for large-scale models, such as a GCM, the LES study is used to determine the PDF of *w*. According to the mathematical definition, if $P(w)dw$ is the probability of w in the interval from w to $w + dw$, then for a continuous w spectrum, the following expression must be satisfied:

$$\int_0^\infty P(w)\, dw = 1. \tag{11}$$

Since the LES model domain contains discrete grid boxes, the following definition of $P(w)$ can be used to evaluate the model-predicted distribution of vertical velocities (Siegel and Morgan 1988):

$$P(w) = \frac{dN(w)}{dV\, dw}, \tag{12}$$

where $dN(w)$ represents the number of grid cells that have vertical velocities in the interval between w and $w + dw$, dV is the total number of grid cells within the model domain, and dw is the sampling threshold. In this study, dw has a value of 0.01 (0.05) m s^{-1} for LES-1 (LES-2).

Figure 12 shows the PDF at 8775 m above sea level (ASL) (corresponding to the interior of the cloud) at 60 min into the simulation. The PDFs for this simulation were quite uniform throughout the cloud layer, with most of the model-predicted vertical velocities falling into a narrow band between -0.1 and 0.05 m s^{-1} (not shown). This is because the TKE for this cloud system was very small, thus vertical variation of TKE had no significant impact on the variation of PDFs. Also, the PDFs follow an approximately normal distribution

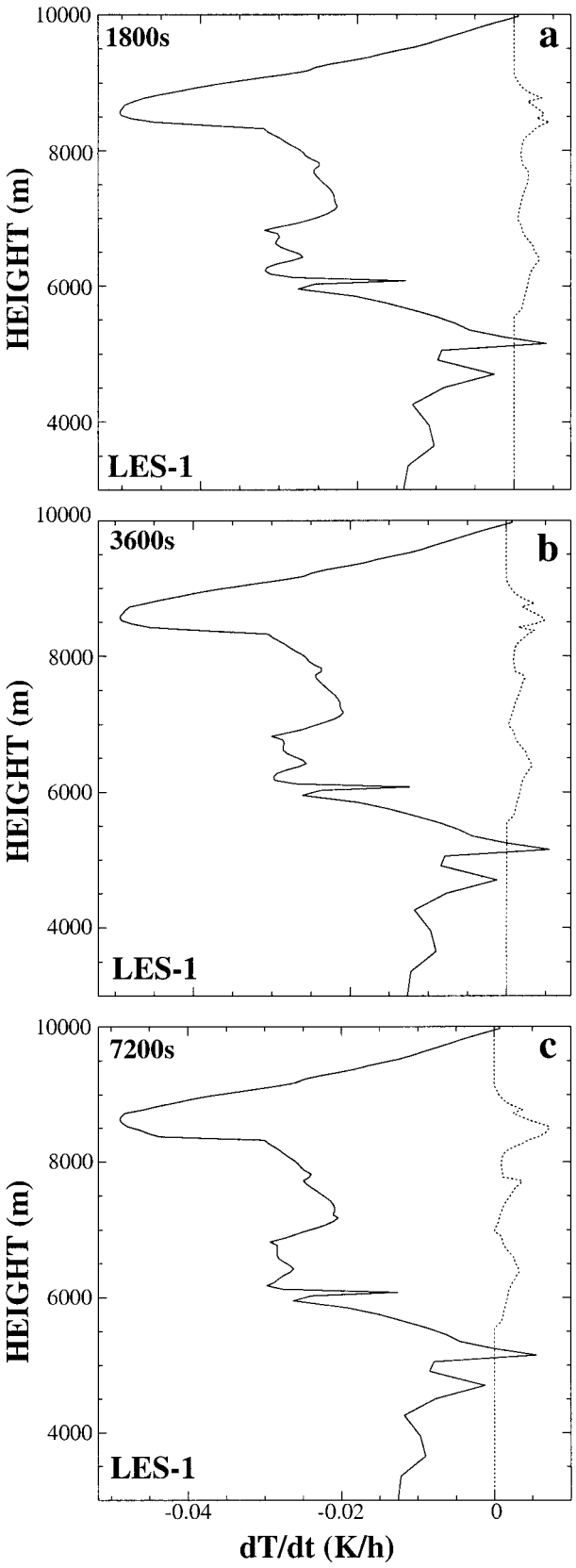

FIG. 11. Profiles of latent (dotted) and total radiative (solid) heating rates at (a) 30 min, (b) 60 min, and (c) 120 min into the simulation for LES-1.

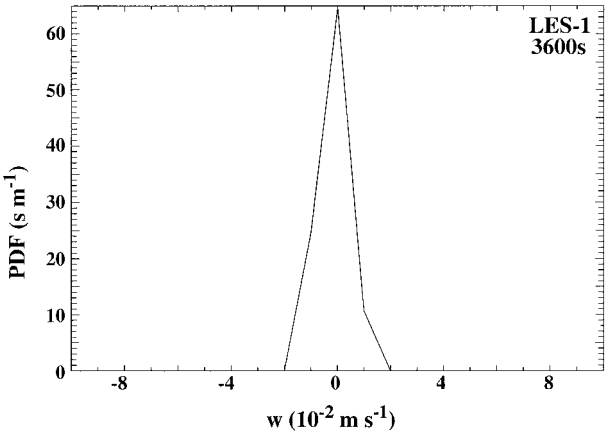

FIG. 12. PDF of w at 8775 m ASL at 60 min into the simulation for LES-1.

throughout the cloud system for this simulation (figure not shown).

7. LES results: LES-2 (deep cloud system)

a. Simulation overview

The 2-h 3D LES for LES-2 was initialized with a sounding taken at 1930 UTC 26 November 1991 (Fig. 4b) from the finest grid of case 2 in the mesoscale simulation (Fig. 1b). As stated previously, the sounding used in this simulation was taken from a deep and active cloud layer from the mesoscale simulation in Wu (1999).

Active cells are seen in the vertical cross-sectional plots along $X = -0.08$ km (Figs. 13–15), similar to those observed by Mace et al. (1995). Generally, the cells in the horizontal cross sections (not shown) had a horizontal extent (in the y direction) less than 2 km and vertical extent less than 1.5 km. This range of cell sizes is comparable to the results in Gultepe et al. (1995). The comparable horizontal and vertical scales for the cells suggest that the eddies were both buoyancy-driven and shear-driven (Stull 1988). A deep cloud system extending from 3.9 to about 9 km was simulated at 2130 UTC, similar to Mace et al.'s (1995) observations. Figures 14a–c can be considered as snapshots of Mace et al.'s (1995) Fig. 16. The upper part of the cloud layer, centered at about 8 km, had larger amounts of PI particles (both in number and mass), while larger snow particle number and mass were in the lower cloud layer, which had its bottom boundary as low as 3.5 km ASL. The maximum number of PI particles nucleated at 30 min into the simulation was 400 L^{-1}, about half of what was observed over Coffeyville 2 h before LES-2 passed

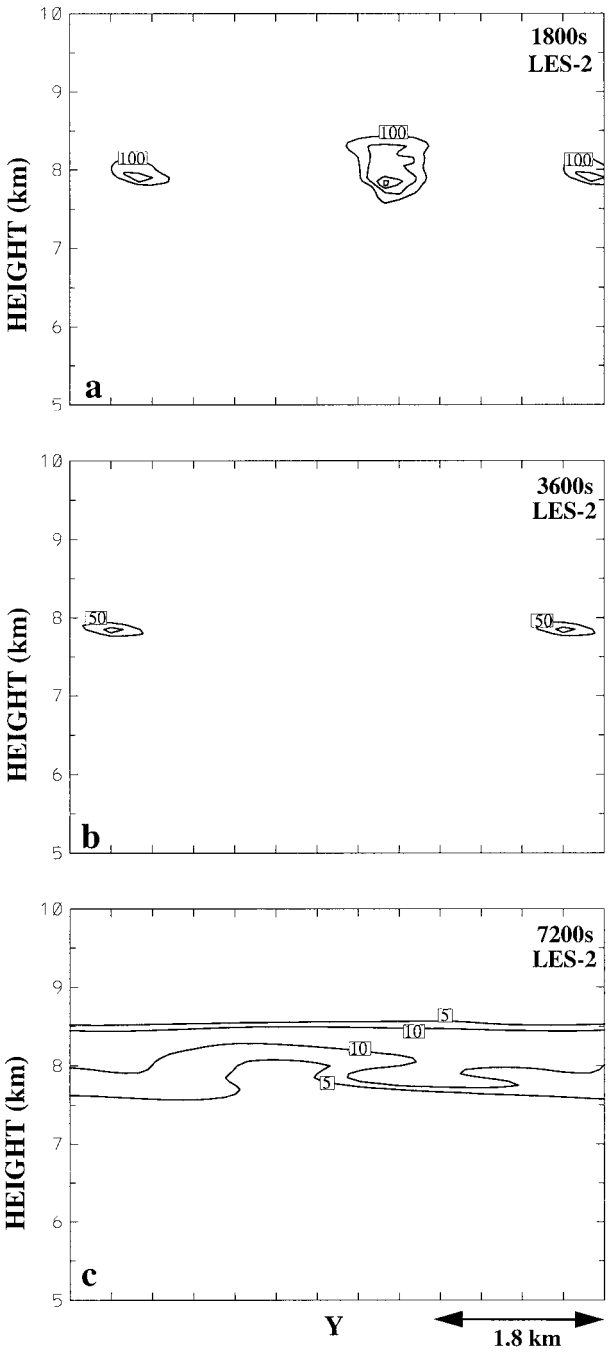

FIG. 13. Vertical *y*–*z* cross section (at $x = -0.08$ km) of pristine ice number concentration for LES-2 at (a) 30 min (at contour intervals of 100 L^{-1}), (b) 60 min (at contour intervals of 50 L^{-1}), and (c) 120 min (at contour intervals of 5 L^{-1}) into the simulation.

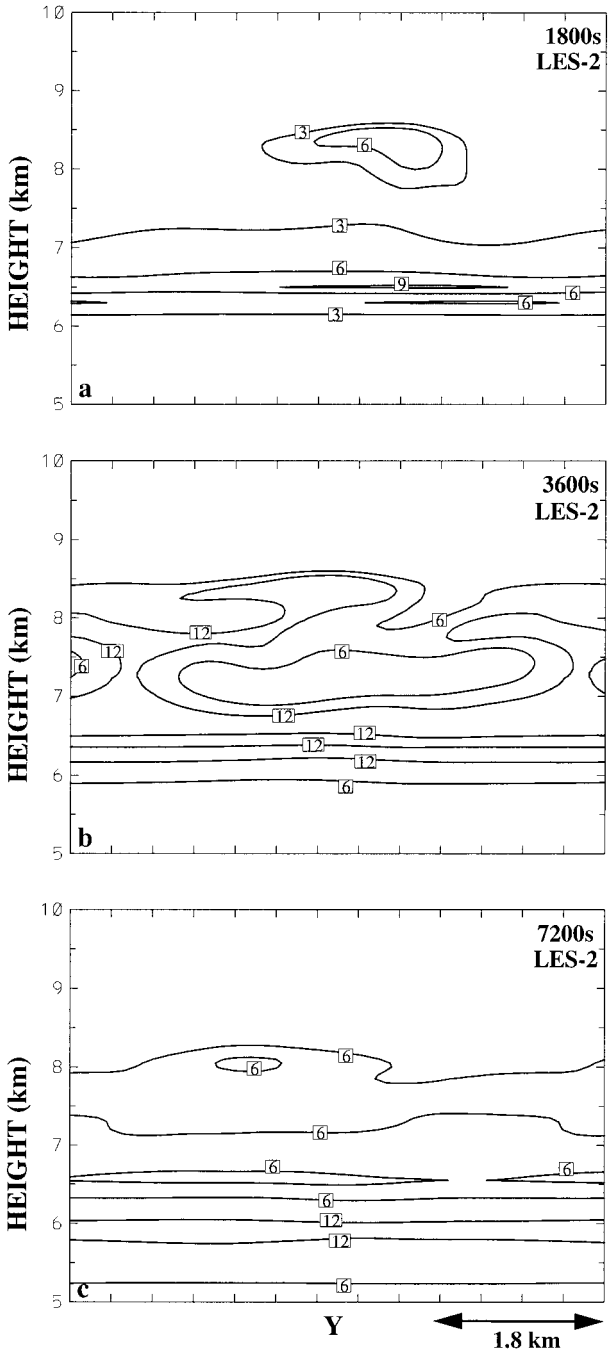

FIG. 14. Vertical *y*–*z* cross section (at $x = -0.08$ km) of snow particle number concentration for LES-2 at (a) 30 min (at contour intervals of 3 L^{-1}), (b) 60 min (at contour intervals of 6 L^{-1}), and (c) 120 min (at contour intervals of 6 L^{-1}) into the simulation.

over that location (Miloshevich 2000). The maximum PI mixing ratio over the course of the simulation was 1.8×10^{-2} g kg^{-1} (figure not shown). Snow particle number concentrations were generally less than 20 L^{-1}, and snow mixing ratios were as large as 1.08×10^{-1} g kg^{-1} (figure not shown). The predicted vertical air velocities along the cross section at 30 min into the simulation ranged from -2.0 to 0.8 m s^{-1}. The magnitude of the vertical air velocity is acceptable for a more convective cirrus cloud (Heymsfield 1977). In addition, the relative large PI and snow concentrations and mixing ratios can be attributed to the larger vertical velocity.

Shown in Fig. 16 are the vertical profiles of layer-

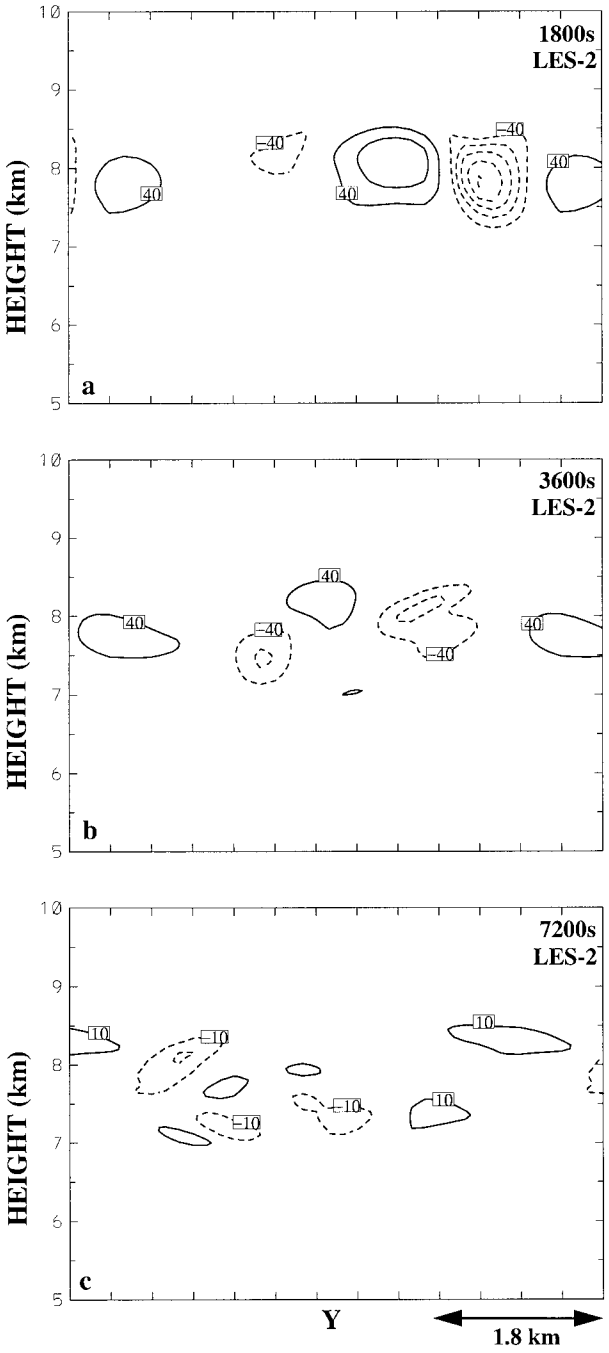

FIG. 15. Vertical y–z cross section (at $x = -0.08$ km) of vertical velocity (w) for LES-2 at (a) 30 min (at contour intervals of 40 cm s^{-1}), (b) 60 min (at contour intervals of 40 cm s^{-1}), and (c) 120 min (at contour intervals of 10 cm s^{-1}) into the simulation.

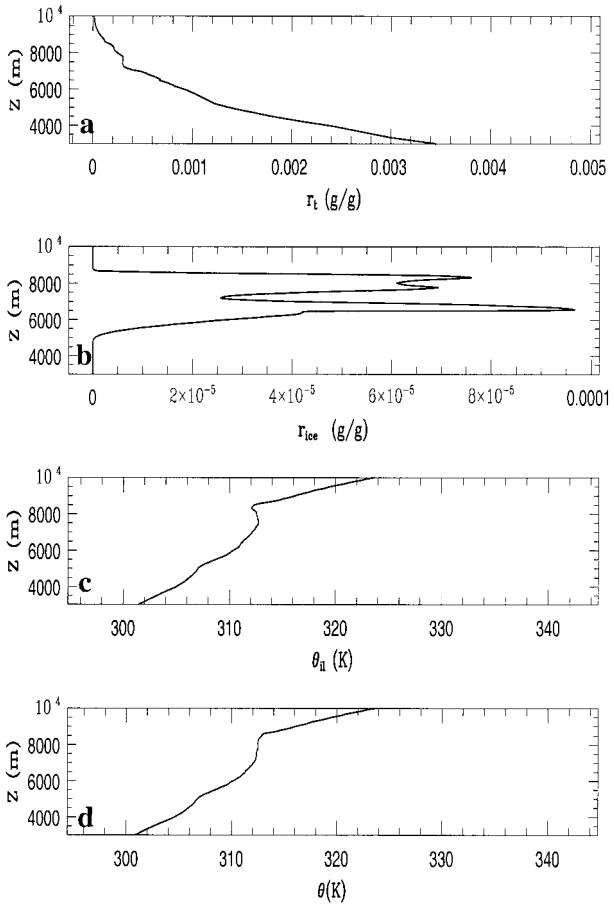

FIG. 16. Profiles of horizontally averaged (a) total water mixing ratio (r_t), (b) total ice mixing ratio (r_{ice}), (c) ice–liquid–water potential temperature (θ_{il}), and (d) potential temperature (θ) at 60 min into the simulation for LES-2.

averaged r_t, r_{ice}, θ_{il}, and θ at 60 min into the simulation. As expected, r_t generally decreased with height, even though the profile was slightly modified due to the existence of condensate in the cloud. The r_{ice} profiles display two maxima (the two maxima at 7500 m and 8500 m can be considered as a single maximum because of their proximity), with the top maxima containing less total ice than below. The maximum total ice for the middle-level cloud layer was slightly less than 0.1 g kg^{-1} at 60 min into the simulation. Although the total ice mixing ratio peaks were located higher in elevation than in observation, this amount was in the right order of magnitude as seen in Mace et al. (1995; Fig. 21), when LES-2 passed over Coffeyville. An unstable layer can be identified in the θ_{il} profile. This unstable layer was responsible for the active turbulent eddies predicted in this case. The unstable layer originated in the initial condition (Fig. 4b), where a deep saturated layer of 100-hPa deep (between 320 and 420) was located beneath a layer of dry air.

The pristine ice started growing via the rosette mode (94.7%) at 30 min of the model time, followed by 4.7% growing by the column mode and less than 1% growing by the needle and hexagonal plate modes. In addition, at 30 min of model time, 57.0% of the snow particles grew via the rosette mode, followed by the needle mode with 33.4% and the column mode by 9.6% (Table 5). The dominance of the rosette habit is indicative of cold temperature (less than 31°C and high ice supersatura-

tion) (see Meyers et al. 1997). Heymsfield and Miloshevich (1995) also found the ice habit to be dominated by the rosette mode at 2025 UTC 26 November 1991 at Coffeyville, 2 h before LES-2 arrived there. Ou et al. (1995) also observed rosettes for this period. As the simulation progressed, less pristine ice and snow particles grew via the rosette mode. By the end of the simulation, virtually all of the pristine ice particles grew via the column mode, and 59.0% of the snow particles grew by the column mode, followed by the needle mode at 23.1% and the hexagonal plate mode by 17.9%. The dominance of the column habit is indicative of the reduction of the ice supersaturation due to the growth of the ice crystals. At 120 min of the model time, the maximum median diameter for snow reached 180 μm, close to the results of Miloshevich (2000) at Coffeyville (2025 UTC 26 November 1991, 2 h before LES-2 reached the site).

The TKE profiles in Fig. 17a show that turbulent eddies were more active in LES-2 than in LES-1. The maximum TKE in LES-2 at 1 h into the simulation was about 0.55 m^2 s^{-2}, which was nearly 200 times the maximum value predicted in LES-1 (Fig. 9a). As the simulation proceeded, transport of TKE both upward and downward can be clearly identified. In addition, the horizontal and vertical TKE were of comparable magnitude (Figs. 17a,b), as seen in more turbulent cirrus clouds (Smith and Jonas 1996).

Similar to what is seen in LES-1, infrared cooling outweighed solar warming, resulting in net radiative cooling in most of the cloud system (Fig. 18a). The maximum net cooling near the cloud top was about three times that of LES-1. However, below 8 km, net radiative cooling or warming was very small. Because a large number of small ice particles were suspended near the cloud top, both solar optical and infrared optical extinctions peaked at 8.5 km ASL (Fig. 18b).

Vertical profiles of the total radiative and latent heating rates are shown in Fig. 19. The change in scale of the horizontal axis between LES-1 and LES-2 demonstrates that latent heating release played a much more significant role in LES-2 than in LES-1 (Fig. 11). The maximum latent heating rate of 0.85 K h^{-1} in the early stage of the cloud development was more than two orders of magnitude greater than that for LES-1 (only about 0.05 K h^{-1}). Two regions of positive latent heating at 30 min of model time corresponded to the two cloud layers described previously. A patch of net evaporation appeared between the two cloud layers after about 1h into the simulation. Net latent heating outweighed the net radiative effect in the cloud development. Latent heat release can destablize the cloud layer, resulting in the formation of convective cells, which are very effective in transporting momentum, heat, and moisture. By the end of the simulation, net radiative cooling dominated at the cloud top region at a maximum rate of about 0.14 K h^{-1}, and the bottom levels of the cloud were dominated by net evaporation, even though strong latent heating was still present in the top cloud layer.

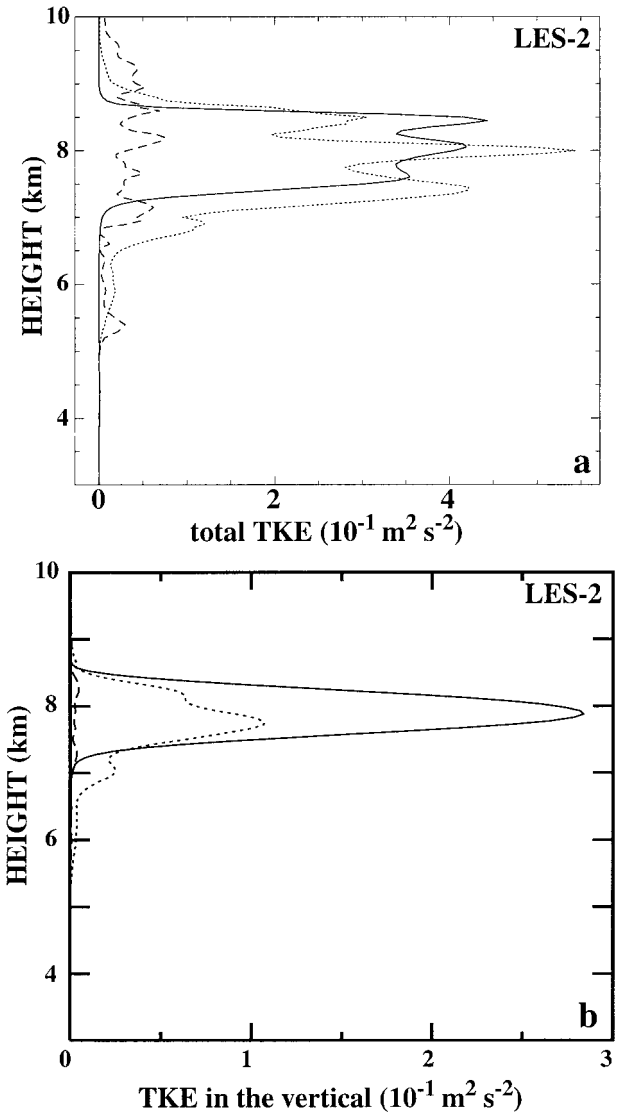

FIG. 17. (a) Profiles of horizontally averaged turbulent kinetic energy (TKE) at 30 min (solid), 60 min (dotted), and 120 min (dashed); (b) profiles of horizontally averaged vertical TKE ($\frac{1}{2}\langle w'w'\rangle$) at 30 min (solid), 60 min (dotted), and 120 min (dashed) into the simulation for LES-2.

b. PDFs of w

The LES-predicted PDFs of w for this case demonstrated distinct features that differed from those in LES-1. From Fig. 20, at the middle-cloud level (7700 m) corresponding to active turbulent motions deep in the cloud system, the PDF had a wider distribution than levels above and below (not shown). Even though the PDFs near the cloud base and top followed an approximate normal distribution with a single peak near $w = 0$, multiple peaks were found in the PDF at the middle

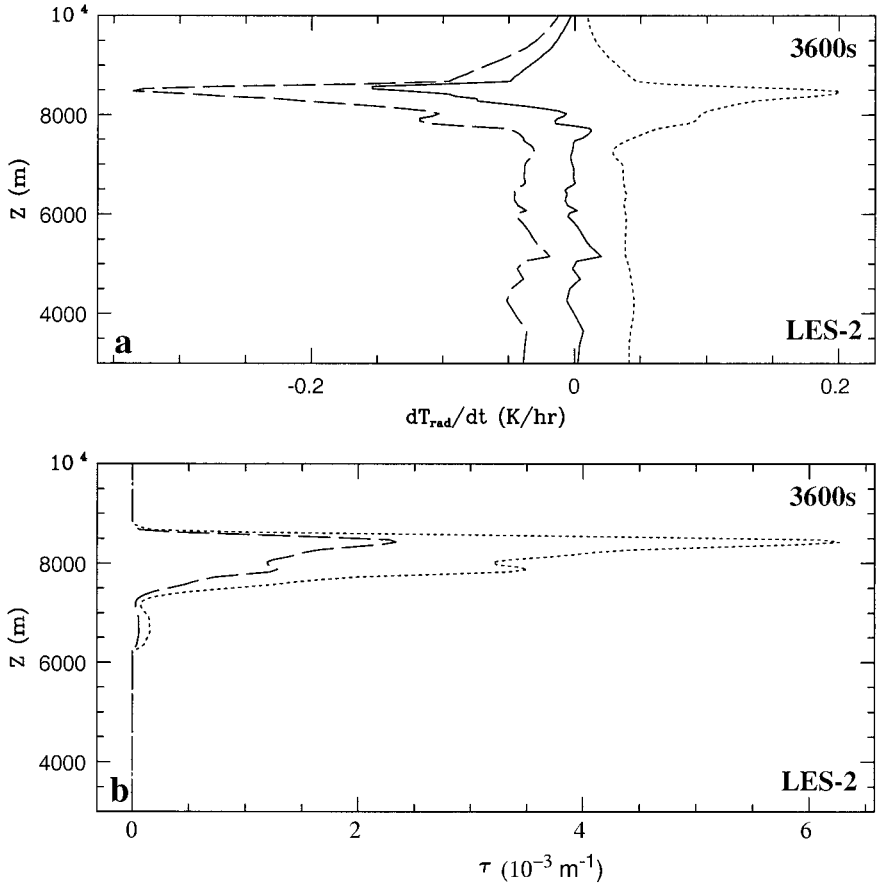

FIG. 18. (a) Profiles of radiative heating rate (solid line: total; dashed line: IR; dotted line: solar) and (b) solar (τ_{solar}) and infrared ($\tau_{infrared}$) optical extinctions (dashed line: IR; dotted line: solar) at 60 min into the simulation for LES-2.

cloud levels. It should be pointed out that the wide PDF distribution deep in the cloud system was associated with buoyancy-driven turbulence because the cloud layer between 7200 and 8500 m was unstable (Fig. 16), especially in the early stage of the simulation. At the early stage of the simulation, the PDF at the middle cloud level covered an even wider *w* spectrum in the downward motion regime than that calculated later in the simulation. Although the PDF spectrum at the middle cloud levels narrowed subsequently in the simulation (not shown), the multiple peaks and fine structures indicated that turbulent eddies were very active within the cloud system because both upward and downward motions were nearly equal (Fig. 20).

8. Discussion and summary

The LES model successfully simulated a single cloud layer for LES-1 and a deep cloud structure for LES-2. Midlatitude cirrus clouds usually form in a stably stratified environment with large-scale forcing (Heymsfield 1977). In spite of the latent heat release during the phase change, there was generally insufficient heating for cirrus clouds in LES-1 to become positively buoyant. Also, the strong temperature inversion at the tropopause provided a lid to prevent cirrus clouds in LES-1 from developing into a deep cloud. As a result, the clouds in LES-1 behaved as quasipassive tracers of the motions in the top of the troposphere. This kind of cirrus cloud can be named *passive cirrus* because of quasipassive tracer properties. However, in some special cases, such as LES-2, positively buoyant cells can be embedded in the cirrus layers. These cells in LES-2 were so active that the rising updraft induced its own pressure perturbations, affecting the cloud evolution. This kind of cirrus can be classified as *active cirrus.*

To determine whether gravity waves were present in the simulation, we show the time–height cross section of *w* near the center of the domain in Fig. 21. In LES-1, a slantwise propagation of the phase of *w* was evident in the first hour of integration, much like an internal gravity wave (Holton 1992). The gravity wave in LES-1 was probably caused by the vertical shear of the horizontal wind around 7.5 km ASL; the level of the vertical shear of the horizontal wind also corresponded to the level from where the gravity waves emanated (Figs. 21a

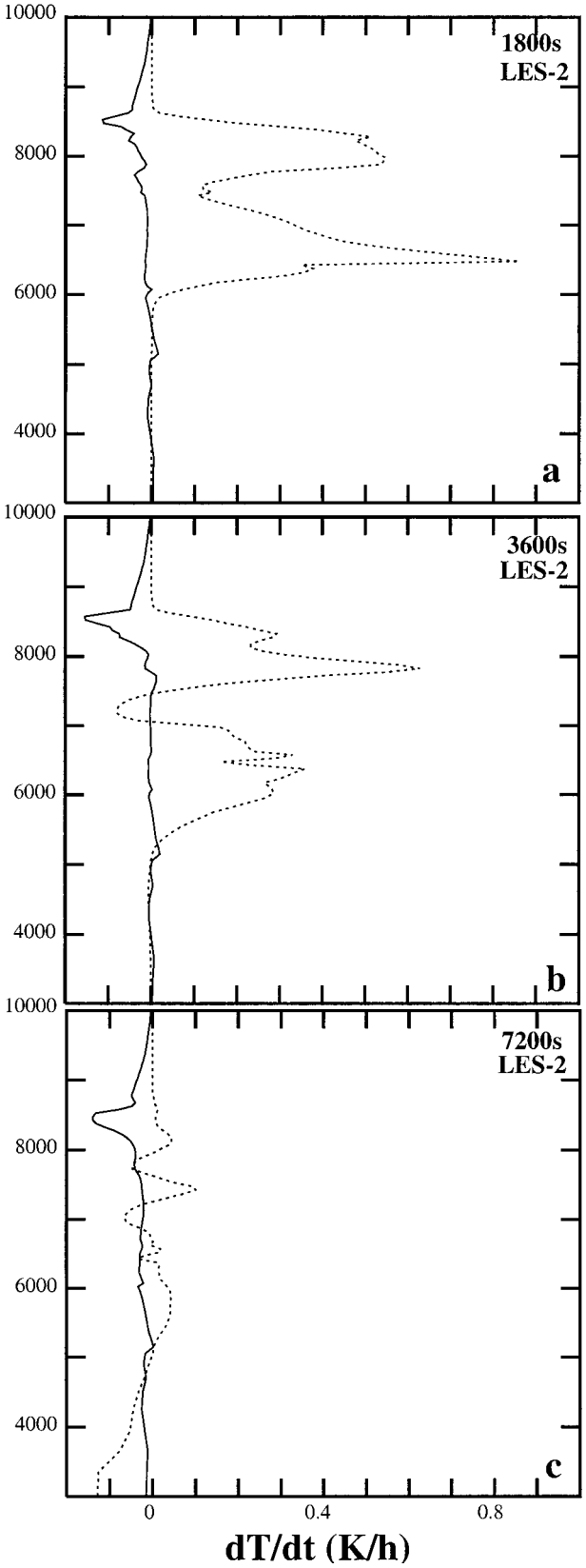

FIG. 19. Profiles of latent (dotted) and total radiative (solid) heating rates at (a) 30 min, (b) 60 min, and (c) 120 min into the simulation for LES-2.

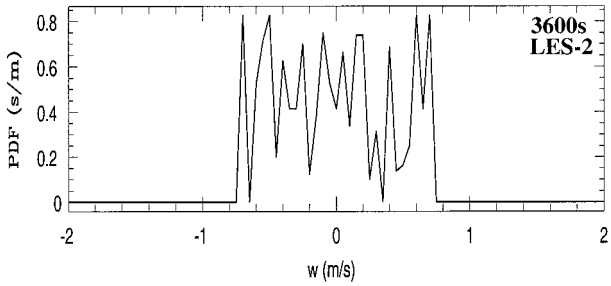

FIG. 20. PDF of w at 7700 m ASL at 60 min into the simulation for LES-2.

and 22a). However, in LES-2, gravity waves did not seem to be present; this was probably due to lower static stability and more turbulence in the flow. Even though there was vertical shear of the horizontal wind in LES-2, we did not detect gravity waves due to the effects of strong turbulent motion (Figs. 21b, 22b).

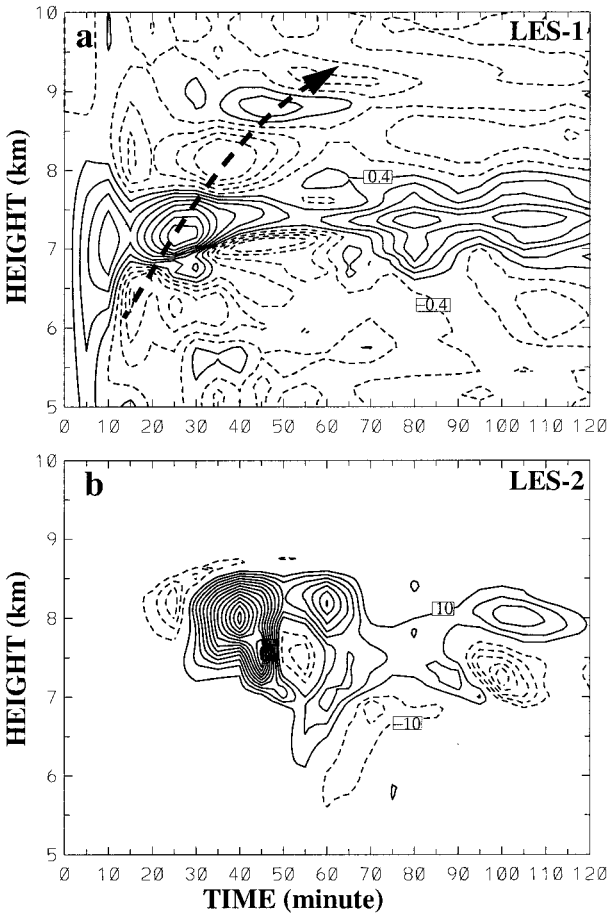

FIG. 21. The height–time cross section of w (in units of 1 cm s^{-1}) at $x, y = -0.08$ km of the model domain for (a) LES-1 at contour intervals of 0.4 cm s^{-1}. Thick dashed line denotes the phase propagation of the gravity waves; (b) LES-2 at contour intervals of 10 cm s^{-1}. Solid (dashed) contours represent positive (negative) values, and zero-contours are suppressed.

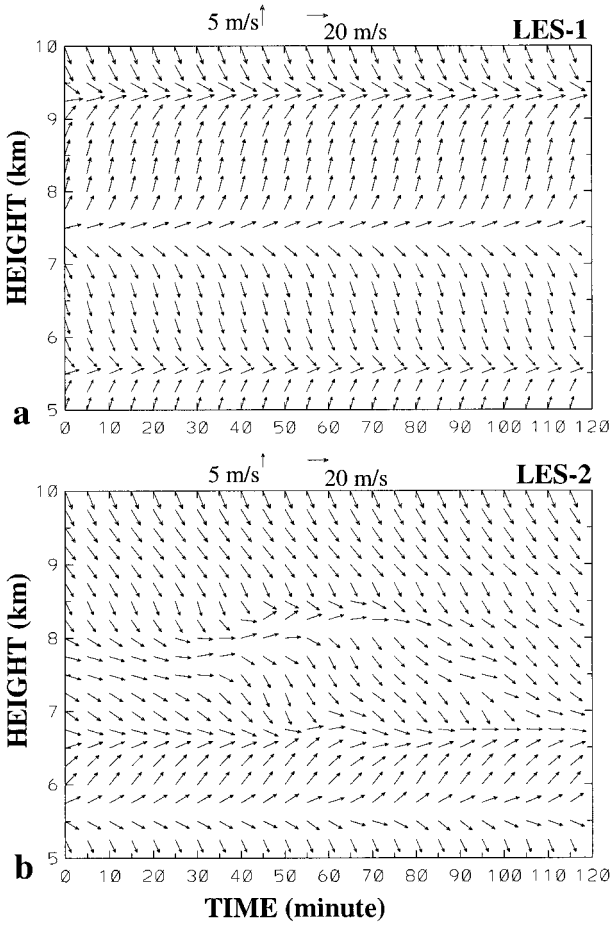

FIG. 22. The height–time cross section of the horizontal wind (in m s^{-1}) at x, $y = -0.08$ km of the model domain for (a) LES-1 and (b) LES-2. The scales of the u and v component of the wind are given at the top of the figure.

Latent heat release can play a significant role in the formation and development of cirrus clouds (Fig. 19). The release of latent heat can be an energy source for the development of upward motions, which, in turn, can produce more supersaturation and cloud development. Vertical profiles of the total radiative and latent heating rates (Figs. 11 and 19) indicate that for well-developed, deep, and active cirrus clouds, radiative cooling and latent heating can be comparable in magnitude in the cloudy layer, as in LES-2 (see Fig. 21b). This implies that latent heating cannot be neglected in the construction of a cirrus cloud model, even though Lilly (1988) had reasonable success with his mixed-layer model in a study of an optically thick cirrus anvils with latent heating ignored. However, for shallow, optically thin cirrus clouds, as in LES-1, the latent heat release can be much smaller than the radiative cooling. In this case, cloud development and evolution are modulated mainly by radiative effects, and latent heat effects can be safely neglected in cirrus cloud models. Gravity waves, however, may provide another uplifting mechanism for cloud development. Generally, the LES studies in this research support Starr and Cox's (1985a,b) model calculations in which the authors showed that latent heating associated with depositional growth and sublimation of ice crystals can be a significant factor in modulating cirrus cloud evolution.

Finally, we have examined the probability density function of w with an eye toward parameterizing cirrus cloud-scale vertical velocities in larger-scale models. We find that the PDFs of w can be approximated by a normal density function for the more radiatively driven thin cirrus case. However, in the interior of the deep, convectively unstable case, the PDFs of w are multimodal and very broad, indicating that parameterizing cloud-scale motions for such clouds can be very challenging.

Acknowledgments. This work was supported by the NASA under contracts #NAG-1-1703 and #NAG-1-2045. The help of Brenda Thompson in preparing this manuscript is much appreciated. We also thank Dr. A. Heymsfield and two anonymous reviewers for their comments, which significantly improved the clarity of the manuscript. We are grateful to Prof. Gerald Mace for providing the optical depth figure. In addition, thanks go to Chris Golaz and Dr. Bob Walko for technical assistance.

REFERENCES

Benjamin, S. G., K. A. Brewster, R. Brummer, B. F. Jewett, T. W. Schlatter, T. L. Smith, and P. A. Stamus, 1991: An isentropic three-hourly data assimilation system using ACARS aircraft observations. *Mon. Wea. Rev.,* **119,** 888–906.

Cotton, W. R., and R. A. Anthes, 1989: *Storm and Cloud Dynamics.* Academic Press, 883 pp.

DeMott, P. J., M. P. Meyers, and W. R. Cotton, 1994: Parameterization and impact of ice initiation processes relevant to numerical model simulations of cirrus clouds. *J. Atmos. Sci.,* **51,** 77–90.

Gultepe, I., and G. V. Rao, 1993: Moisture and heat budgets of a cirrus cloud from aircraft measurements during FIRE. *Quart. J. Roy. Meteor. Soc.,* **119,** 957–974.

——, and D. O'C. Starr, 1995a: A comparison of evaporative cooling with infrared heating beneath a cirrus cloud. *J. Atmos. Res.,* **35,** 217–231.

——, and ——, 1995b: Dynamical structure and turbulence in cirrus clouds: Aircraft observations during FIRE. *J. Atmos. Sci.,* **52,** 4159–4182.

——, ——, A. J. Heymsfield, T. Uttal, T. P. Ackerman, and D. L. Westpal, 1995: Dynamic characteristics of cirrus clouds from aircraft and radar observations in micro and meso-γ scales. *J. Atmos. Sci.,* **52,** 4060–4078.

——, I. G. Issac, D. Hudak, R. Nissen, and J. W. Strapp, 2000: Dynamical and microphysical characteristics of Arctic clouds during BASE. *J. Climate,* **13,** 1225–1254.

Harrington, J. Y., 1997: The effects of radiative and microphysical processes on simulated warm and transition-season Arctic stratus. Ph.D. dissertation, Colorado State University, Fort Collins, CO, 270 pp.

——, M. P. Meyers, R. L. Walko, and W. R. Cotton, 1995: Parameterization of ice crystal conversion processes due to vapor deposition for mesoscale models using double-moment basis functions. Part I: Basic formulation and parcel model results. *J. Atmos. Sci.,* **52,** 4344–4366.

——, T. Reisin, W. R. Cotton, and S. M. Kreidenweis, 1999: Cloud

resolving simulations of Arctic stratus. Part II: Transition-season clouds. *Atmos. Res.*, **51,** 45–75.

Heymsfield, A. J., 1977: Precipitation development in stratiform ice clouds: A microphysical and dynamical study. *J. Atmos. Sci.*, **34,** 367–381.

——, and L. M. Miloshevich, 1995: Relative humidity and temperature influences on cirrus formation and evolution: Observations from wave clouds and FIRE II. *J. Atmos. Sci.,* **52,** 4302–4326.

——, ——, G. M. McFarquhar, and S. Aulenbach: Nonspherical ice particles in cirrus clouds. Preprints, *Conf. on Light Scattering by Nonspherical Particles: Theory, Measurements, and Applications*, New York, NY, Amer. Meteor. Soc., 36–39.

Holton, J. R., 1992: *An Introduction to Dynamic Meteorology.* 3d ed. Academic Press, 511 pp.

Kosovic, B., 1996: Subgrid-scale modeling for the large-eddy simulation of stably stratified boundary layers. Ph.D. thesis, Department of Aerospace Engineering Sciences, University of Colorado, Boulder, CO, 253 pp.

——, 1997: Subgrid-scale modelling for the large-eddy simulation of high Reynolds number boundary layers. *J. Fluid Mech.*, **336,** 151–182.

Kristjánsson, J. E., J. M. Edwards, and D. L. Mitchell, 2000: Impact of new scheme for optical properties of ice crystals on climate of two GCMs. *J. Geophys. Res.,* **105,** 10 063–10 079.

Lilly, D. K., 1988: Cirrus outflow dynamics. *J. Atmos. Sci.,* **45,** 1594–1605.

Liou, K. N., 1986: Influence of cirrus clouds on weather and climate process: A global perspective. *Mon. Wea. Rev.,* **114,** 1167–1199.

Louis, J. F., 1979: A parametric model of vertical eddy fluxes in the atmosphere. *Bound.-Layer Meteor.,* **17,** 187–202.

Mace, G. G., D. O'C. Starr, T. P. Ackerman, and P. Minnis, 1995: Examination of coupling between an upper-tropospheric cloud system and synoptic-scale dynamics diagnosed from wind profiler and radiosonde data. *J. Atmos. Sci.,* **52,** 4094–4127.

Meyers, M. P., P. J. DeMott, and W. R. Cotton, 1992: New primary ice nucleation parameterizations in an explicit cloud model. *J. Appl. Meteor.*, **31,** 708–721.

——, R. L. Walko, J. Y. Harrington, and W. R. Cotton, 1997: New RAMS cloud microphysics parameterization. Part II: The two-moment scheme. *Atmos. Res.*, **45,** 3–39.

Miloshevich, L. M., 2000: NCAR ice crystal replicator data. [Available online at http://box.mmm.ucar.edu:80/science/cirrus.]

Mitchell, D. L., and W. P. Arnott, 1994: A model predicting the evolution of ice particle size spectra and radiative properties of cirrus clouds. Part II: Depedence of absorption and extinction on ice crystal morphology. *J. Atmos. Sci.*, **51,** 817–832.

——, A. Macke, and Y. Liu, 1996: Modeling cirrus clouds. Part II: Treatment of radiative properties. *J. Atmos. Sci.,* **53,** 2967–2988.

Moeng, C.-H., 1984: A large-eddy-simulation model for the study of planetary boundary-layer turbulence. *J. Atmos. Sci.,* **41,** 2052–2062.

Moncrieff, M. W., S. K. Krueger, D. Gregory, J.-L. Redelsperger, and W.-K. Tao, 1997: GEWEX cloud system study (GCSS) working group 4: Precipitating convective cloud systems. *Bull. Amer. Meteor. Soc.*, **78,** 831–845.

Ou, S. C., and Coauthors, 1995: Remote sounding of cirrus cloud optical depths and ice crystal sizes from AVHRR data: Verification using FIRE II IFO measurements. *J. Atmos. Sci.*, **52,** 4143–4158.

Pielke, R. A., and Coauthors, 1992: A comprehensive meteorological modeling system—RAMS. *Meteor. Atmos. Phys.*, **49,** 69–91.

Siegel, A. F., and C. J. Morgan, 1988: *Statistics and Data Analysis: An Introduction.* 2d ed. John Wiley and Sons, 635 pp.

Smith, S. A., and P. R. Jonas, 1996: Observations of turbulence in cirrus clouds. *Atmos. Res.,* **43,** 1–29.

Starr, D. O'C., and S. K. Cox, 1985a: Cirrus clouds. Part I: A cirrus cloud model. *J. Atmos. Sci.,* **42,** 2663–2681.

——, and ——, 1985b: Cirrus clouds. Part II: Numerical experiments on the formation and maintenance of cirrus. *J. Atmos. Sci.,* **42,** 2682–2694.

——, and D. P. Wylie, 1990: The 27–28 October 1986 FIRE cirrus case study: Meteorology and clouds. *Mon. Wea. Rev.,* **118,** 2259–2287.

Stull, R. B., 1988: *An Introduction to Boundary Layer Meteorology.* Kluwer Academic, 666 pp.

Tripoli, G. J., and W. R. Cotton, 1982: The Colorado State University Three-Dimensional Cloud/Mesoscale Model. Part I: General theoretical framework and sensitivity experiments. *Atmos. Res.,* **18,** 185–219.

Walko, R. L., W. R. Cotton, M. P. Meyers, and J. Y. Harrington, 1995: New RAMS cloud microphysics parameterization. Part I: The single-moment scheme. *Atmos. Res.*, **38,** 29–62.

Wu, T., 1999: Numerical modeling study of the November 26, 1991 cirrus event. Ph.D. dissertation, Colorado State University, Fort Collins, CO, 186 pp.